

The physical origin for spatially large scatter of IGM opacity at the end of reionization: the IGM Ly α opacity-galaxy density relation

Rikako Ishimoto^{1*}, Nobunari Kashikawa^{1,2}, Daichi Kashino³, Kei Ito^{1,4,5}, Yongming Liang^{4,5}, Zheng Cai⁶, Takehiro Yoshioka¹, Katsuya Okoshi⁷, Toru Misawa⁸, Masafusa Onoue^{9,10,11}, Yoshihiro Takeda¹, and Hisakazu Uchiyama¹²

¹Department of Astronomy, Graduate School of Science, The University of Tokyo, 7-3-1 Hongo, Bunkyo, Tokyo 113-0033, Japan

²Research Center for the Early Universe, The University of Tokyo, 7-3-1 Hongo, Bunkyo-ku, Tokyo 113-0033, Japan

³Institute for Advanced Research, Nagoya University, Furocho, Chikusa-ku, Nagoya, 464-8601, Japan

⁴Department of Astronomical Science, Graduate University for Advanced Studies (SOKENDAI), Mitaka, Tokyo 181-8588, Japan

⁵National Astronomical Observatory of Japan, 2-21-1 Osawa, Mitaka, Tokyo 181-8588, Japan

⁶Department of Astronomy and Tsinghua Center for Astrophysics, Tsinghua University, Beijing 100084, China

⁷Institute of Arts and Sciences, Tokyo University of Science, 6-3-1, Niijyuku, Katsushika, Tokyo 125-8585, Japan

⁸School of General Studies, Shinshu University, 3-1-1, Asahi, Matsumoto City 390-8621, Japan

⁹Max-Planck-Institut für Astronomie, Königstuhl 17, D-69117 Heidelberg, Germany

¹⁰Kavli Institute for Astronomy and Astrophysics, Peking University, Beijing 100871, China

¹¹Kavli Institute for the Physics and Mathematics of the Universe (WPI), University of Tokyo, Kashiwa, Chiba 277-8583, Japan

¹²Research Center for Space and Cosmic Evolution, Ehime University, Matsuyama, Ehime 790-8577, Japan.

Accepted XXX. Received YYY; in original form ZZZ

ABSTRACT

The large opacity fluctuations in the $z > 5.5$ Ly α forest may indicate inhomogeneous progress of reionization. To explain the observed large scatter of the effective Ly α optical depth (τ_{eff}) of the intergalactic medium (IGM), fluctuation of UV background (Γ model) or the IGM gas temperature (T model) have been proposed, which predict opposite correlations between τ_{eff} and galaxy density. In order to address which model can explain the large scatter of τ_{eff} , we search for Ly α emitters (LAEs) around two (J1137+3549 and J1602+4228) quasar sightlines with $\tau_{\text{eff}} \sim 3$ and J1630+4012 sightline with $\tau_{\text{eff}} \sim 5.5$. Using a narrowband imaging with Subaru/Hyper Suprime-Cam, we draw LAE density maps to explore their spatial distributions. Overdensities are found within $20 h^{-1}$ Mpc of the quasar sightlines in the low τ_{eff} regions, while a deficit of LAEs is found in the high τ_{eff} region. Although the τ_{eff} of the three quasar sightlines are neither high nor low enough to clearly distinguish the two models, these observed τ_{eff} -galaxy density relations all consistently support the Γ model rather than the T model in the three fields, along with the previous studies. The observed overdensities near the low τ_{eff} sightlines may suggest that the relic temperature fluctuation does not affect reionization that much. Otherwise, these overdensities could be attributed to other factors besides the reionization process, such as the nature of LAEs as poor tracers of underlying large-scale structures.

Key words: dark ages, reionization, first stars – intergalactic medium – galaxies: high-redshift

1 INTRODUCTION

Exploring the evolution of the intergalactic medium (IGM) provides insights into when and how the cosmic reionization proceeded. The effective Ly α optical depth, τ_{eff} , measured in high- z ($z \gtrsim 6$) quasar spectra is a useful probe of the IGM state, which is defined as

$$\tau_{\text{eff}} = -\ln \langle F \rangle, \quad (1)$$

where F is the observed flux normalized by the intrinsic spectrum. The observations of τ_{eff} have been conducted to investigate the IGM state (Fan et al. 2006; Becker et al. 2015b; Eilers et al. 2018; Yang et al. 2020; Bosman et al. 2022). The recent measurements of τ_{eff} revealed a steep increase in τ_{eff} and its scatter at $z > 5.5$, suggesting a prominent increase in the hydrogen neutral fraction, f_{HI} , and a

spatially patchy reionizing process (Fan et al. 2006; Bosman et al. 2018; Yang et al. 2020; Bosman et al. 2022). However, a physical origin of such a significant variation in Ly α forest opacity at $z > 5.5$ has not yet been identified.

In a photoionized IGM, the ionization equilibrium yields following equation;

$$n_{\text{HI}}\Gamma = n_e n_{\text{HI}} \alpha_{\text{HI}}(T). \quad (2)$$

Here, Γ is the photoionization rate, and n_{HI} , n_{HI} , and n_e are the number densities of neutral hydrogen, ionized hydrogen, and free electrons, respectively. The $\alpha_{\text{HI}}(T)$ is the radiative recombination coefficient, and T is the gas temperature. We adopt $\alpha_{\text{HI}}(T) \propto T^{-0.72}$ (Becker et al. 2015a). Therefore, f_{HI} scales as

$$f_{\text{HI}} \propto n_{\text{HI}} T^{-0.72} \Gamma^{-1}, \quad (3)$$

where n_{H} is the total hydrogen density. Becker et al. (2015b) tried

* E-mail: ishimoto@astron.s.u-tokyo.ac.jp

to reproduce the observed τ_{eff} by the model where the scatter in τ_{eff} between sightlines is driven entirely by variations in the hydrogen density, n_{H} in Equation 3. They showed the observed scatter in τ_{eff} at $z < 5$ is well reproduced by the simulation; however, at higher redshift, the observed scatter spans wider than that predicted by the simulation. Their results suggest that the density fluctuation alone is not sufficient to produce the observed large scatter of τ_{eff} .

Some possible models have been proposed to explain large fluctuation in τ_{eff} . Davies & Furlanetto (2016) built a self-consistent model of the ionizing background that includes fluctuations in the mean free path due to the varying strength of the ionizing background and large-scale density field (Γ model, see also D’Aloisio et al. 2018; Nasir & D’Aloisio 2020). In this model, low-density regions have fewer ionizing sources and a short mean free path, which combine to produce a low ionizing background. This increases the neutral fraction and hence the Ly α opacity.

On the other hand, D’Aloisio et al. (2015) proposed that large temperature fluctuations may produce the observed large scatter of τ_{eff} (T model). In this scenario, overdense regions are the most opaque because the gas densities are higher, and also because these regions are reionized first, allowing them to cool. This means that large τ_{eff} is observed where the galaxy number density is large, contrary to the Γ model.

Another model is that the τ_{eff} scatter is driven by fluctuations of a radiation field dominated by rare, bright sources such as quasars (Chardin et al. 2015, 2017). However, this model requires higher number density of quasars than that estimated from observations (Kashikawa et al. 2015; Onoue et al. 2017; Matsuoka et al. 2019; Jiang et al. 2022; but see Grazian et al. 2022). The model also suggests earlier He II reionization than that expected from observations (D’Aloisio et al. 2017).

More recently, Kulkarni et al. (2019), Keating et al. (2020a,b), and Nasir & D’Aloisio (2020) performed radiative transfer simulations to show that reionization complete at $z \sim 5.3$, and 50% of the volume of the universe is ionized at $z \sim 7$. In their late reionization model, residual neutral gas islands produce the large scatter of Ly α optical depth.

Recently, Davies et al. (2018) demonstrated that observations of the galaxy populations in the vicinity of the quasar sightline can distinguish the two plausible competing models, Γ model and T model. Their simulations predicted that at the sightline with deep Ly α trough, fluctuating ionizing background would show a deficit of galaxies, while, quite the contrary, residual temperature variation would show an overdensity of galaxies. It is thus possible to directly distinguish these two predictions through measuring the galaxy distributions at the same redshift.

Becker et al. (2018) conducted a search for Ly α Emitters (LAEs) at the sightline of ULAS J0148+0600, which has a giant Gunn-Peterson trough (Gunn & Peterson 1965) spanning $110 h^{-1}\text{Mpc}$, and an extremely large Ly α optical depth $\tau_{\text{eff}} \geq 7.2$ (Becker et al. 2015b). They found a significant deficit of $z \approx 5.7$ LAEs within $20 h^{-1}\text{Mpc}$ from the quasar sightline. The result is consistent with the prediction with fluctuating UV background model and disfavored the scenario with fluctuating gas temperature. Kashino et al. (2020) performed a survey of Lyman Break Galaxies (LBGs) at the same ULAS J0148+0600 field. They also found a deficit of galaxies near the trough, consistent with Becker et al. (2018), suggesting that the paucity of the LAEs is not purely due to absorption of Ly α photons, but reflects a real underdensity of galaxies in this field. Christenson et al. (2021) analyzed LAE distribution in another high τ_{eff} region, SDSS J1250+3130 with optical depth $\tau_{\text{eff}} = 5.7 \pm 0.4$, and also found a LAE deficit around the quasar sightline, which are consis-

tent with previous studies. However, these studies carried out galaxy searches for only two sightlines. Any other interpretations including a genuinely LAE low-density region, cannot be rejected. Further observations of other quasar sightlines are needed in order to conclude the trend.

In this work, we newly observe three fields around high- z quasar sightlines with both high and low τ_{eff} at $z \sim 5.7$. Using wide field imaging capability of Hyper Suprime-Cam (HSC; Furusawa et al. 2018; Kawanamoto et al. 2018; Komiyama et al. 2018; Miyazaki et al. 2018) mounted on the Subaru telescope, we conduct LAE search at $z \sim 5.7$ by using narrow-band filter, NB816 in the fields to measure the spatial distribution of LAEs around three sightlines. This work includes the targets with low τ_{eff} , for the first time, to perform the counter test to contrast what we find for them with the results from high τ_{eff} sample, investigating which of the two conflicting models, Γ model and T model can explain the large scatter of τ_{eff} . We compare our results among three fields and the previous studies and discuss the plausible model for the origin of the patchy reionization.

In Section 2, we present our target selection, observation data, its reduction, and the LAE selection. We show our results in Section 3. In Section 4, we discuss the implications obtained from the comparison of our observations with the model, after taking into account the uncertainties of the observational data. Finally, we summarize the paper in Section 5. We assume a Λ CDM cosmology with $\Omega_m = 0.3$, $\Omega_\Lambda = 0.7$, and $h = 0.7$. We use the AB magnitude unless specified otherwise.

2 OBSERVATIONS AND SAMPLE SELECTION

2.1 Target selection

We choose three fields to measure the galaxy density at $z \sim 5.7$ around sightlines of: J1137+3549 and J1602+4228 with low ($\tau_{\text{eff}} \sim 3$) Ly α opacities, and J1630+4012 with high ($\tau_{\text{eff}} \sim 5.5$) opacity at $z = 5.726 \pm 0.046$, which corresponds to the HSC NB816 filter’s wavelength coverage for Ly α emission. These spectra are selected from the publicly available *igmspec*¹ database (Prochaska 2017). The details of observed fields are summarized in Table 1.

There are very few quasars having a high or low Ly α opacity just right at $z \sim 5.7$ on their spectra; therefore these are almost only solutions among the currently available quasars with good quality and high-enough resolution spectra, though there are certainly some errors in the opacity measurements. The detail of the τ_{eff} measurement is described in Section 2.2. The $\tau_{\text{eff}} = 5.47 \pm 0.86$ of J1630+4012 exceeds the 95% range in τ_{eff} predicted by the uniform UV background model from Becker et al. (2015b) and cannot be explained by the density variations alone. On the other hand, for the low- τ_{eff} region, $\tau_{\text{eff}} = 3.07 \pm 0.03, 3.23 \pm 0.05$ are obtained for J1137+3549 and J1602+4228, respectively. To clearly distinguish the Γ model and the T model, it is ideal to choose fields with even lower τ_{eff} than those of J1137+3549 and J1602+4228, although such optimal targets are hard to be found at $z \sim 5.7$. Based on the τ_{eff} distribution at $5.6 < z < 5.8$ (Bosman et al. 2022), the observed $\tau_{\text{eff}} = 3.07$ (J1137+3549) and 3.23 (J1602+4228) correspond to 12, 17 percentile from the bottom, while $\tau_{\text{eff}} = 5.47$ (J1630+4012) corresponds to 5 percentile from the top.

At first, we had measured τ_{eff} over the FWHM ($8120\text{--}8234 \text{ \AA}$, $30 h^{-1}\text{Mpc}$) of NB816 filter as an effective wavelength range, and had found the $\tau_{\text{eff}} = 5.58 \pm 0.62, 6.05 \pm 0.91, \geq 5.06$ for J1137+3549,

¹ <http://specdb.readthedocs.io/en/latest/igmspec.html>

Table 1. Overview of the observed fields

Field	R.A.	Decl.	quasar redshift	redshift references	τ_{eff}
J1137+3549	11 ^h 37 ^m 17 ^s .73	+35°49′56″.9	6.009 ± 0.010	Shen et al. (2019)	3.07 ± 0.03
J1602+4228	16 ^h 02 ^m 53 ^s .98	+42°28′24″.9	6.083 ± 0.005	Shen et al. (2019)	3.23 ± 0.05
J1630+4012	16 ^h 30 ^m 33 ^s .90	+40°12′09″.7	6.065 ± 0.007	Carilli et al. (2010)	5.47 ± 0.86

Notes - The columns show the field name, coordinate, the quasar redshift and its error, the reference for redshift, and Ly α optical depth τ_{eff} . We measure τ_{eff} within 8080–8274 Å, corresponding to $z = 5.65 - 5.81$, 50 h^{-1} Mpc range.

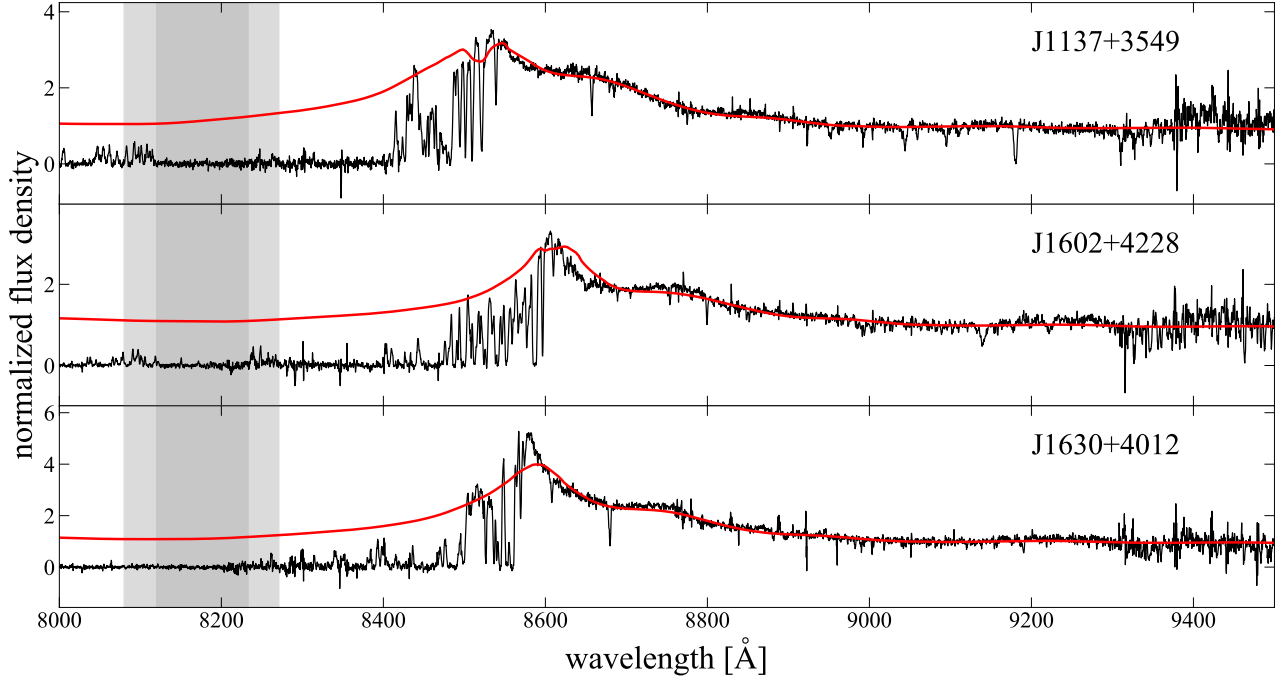


Figure 1. The intrinsic spectra estimated by PCA. The black and red curves show the observed and the predicted spectrum of each quasar, respectively. The light and dark grey regions indicate the wavelength range corresponding to the FWHM of the NB816 filter and the 50 h^{-1} Mpc range, used for the measurement of τ_{eff} . The flux density is normalized by the value at 1280 Å in rest frame.

J1602+4228, and J1630+4012, respectively; therefore, J1137+3549 and J1602+4228 were treated as high τ_{eff} regions. However, when we re-measured more carefully τ_{eff} over 50 h^{-1} Mpc range (8080–8274 Å), which is the same length as that used in the model predictions described later, these two regions have turned out to show low τ_{eff} . Since the spectra of J1137+3549 and J1602+4228 show high transmission just outside of FWHM of NB816 as shown in Figure 1, the τ_{eff} values in these fields are greatly sensitive to the width of the τ_{eff} measurement. This τ_{eff} uncertainty makes the interpretation of results a little more difficult (see Section 4.2). For a fair comparison with the model predictions, we adopt τ_{eff} in 50 h^{-1} Mpc range. While it may be ideal to choose a sightline target where the transmission is almost constant within the sensitivity range of the NB filter so that it is not affected by the width of the τ_{eff} measurement, it is rare to have extremely long Gunn-Peterson troughs or transparent regions as in J0148+0600. Conversely, we would say we are choosing more general sightlines rather than exceptional ones for this study.

2.2 Optical depth measurement

We calculate Ly α optical depth, τ_{eff} , at the wavelength coverage of the NB816 filter. In this part, we present how we estimate intrinsic quasar spectra free from IGM absorption and τ_{eff} , following the same manner as Ishimoto et al. (2020). The spectra cover the wavelength coverage from 3900 to 10000 Å with a resolution of $R \approx 4000$. They are taken from *igmspec* database (Prochaska 2017). All three quasar spectra in this study were acquired with the Keck ESI echelle spectrograph.

We estimate the quasar intrinsic spectra after normalizing at rest 1280 Å with principal component spectra (PCS) from a principal component analysis (PCA) of low- z quasar spectra. This approach is justified by the lack of a significant redshift evolution of quasar spectra in the rest-frame UV wavelength range (e.g., Jiang et al. 2009). In PCA, the quasar spectrum, $q_i(\lambda)$, is modeled as a mean quasar spectrum, $\mu(\lambda)$, and a linear combination of PCS:

$$q_i(\lambda) \sim \mu(\lambda) + \sum_{j=1}^m c_{ij} \xi_j(\lambda), \quad (4)$$

where i refers to a i th quasar, $\xi_j(\lambda)$ is the j th PCS, and c_{ij} is the weight. We use the PCS from [Suzuki et al. \(2005\)](#), which constructed PCS using low- z ($z < 1$) quasars. First, c'_{ij} , the weights for the spectrum redward of 1216\AA , are derived by

$$c'_{ij} = \int_{1216\text{\AA}}^{\lambda_{\text{upper}}} [q_i(\lambda) - \mu(\lambda)] \xi_j(\lambda) d\lambda, \quad (5)$$

where λ_{upper} is the upper limit of available wavelength in each observed quasar spectrum. [Suzuki et al. \(2005\)](#) produced PCS for 1216\AA to 1600\AA , while our sample has coverages up to $\sim 1400\text{\AA}$ in rest frame.

Then we use the projection matrix \mathbf{X} to calculate c_{ij} , the weights for the whole intrinsic spectrum, covering the entire spectral region between 1020\AA and 1600\AA , using

$$c_{ij} = c'_{ij} \cdot \mathbf{X}. \quad (6)$$

The projection matrix \mathbf{X} is also taken from [Suzuki et al. \(2005\)](#). It is the matrix which satisfies the relation $\mathbf{C} = \mathbf{D} \cdot \mathbf{X}$, where \mathbf{C} and \mathbf{D} are the weights of principal components of the whole and the redward of quasar spectrum derived in [Suzuki et al. \(2005\)](#), respectively. We use five PCS for all quasar spectra. The estimated spectra are shown in Figure 1, and the continuum-normalized spectrum of each quasar is shown in Figure 2.

We estimate the effective optical depth τ_{eff} using Equation 1. If the mean normalized flux is negative or is detected less than 2σ significance, we adopt a lower limit of optical depth at $-\ln(2\sigma_{(F)})$. We measure τ_{eff} at $8080 - 8274\text{\AA}$ ($z = 5.65 - 5.81$). This range corresponds to $50 h^{-1}$ Mpc and $> 1\%$ transmission of NB816.

The uncertainty of τ_{eff} is estimated by taking into account the observation error of the spectrum and the uncertainty of the continuum estimation. Errors due to noise in the spectra are estimated by the Monte Carlo simulation using the noise spectra. We generate 100 mock spectra, in which the flux of each spectral pixel is given a random error perturbed within the measured 1σ error, and repeat the continuum estimation and τ_{eff} measurement. The uncertainty of the τ_{eff} from the continuum error due to the measurement error of the quasar redshift is found to be small, about 0.02. However, there are other factors that cause uncertainties in τ_{eff} measurement, which will be verified in Sec 4.1. The measured τ_{eff} and the associated errors are summarized in Table 1.

2.3 Hyper Suprime-Cam Imaging

We use r , i , z , and NB816 imaging data, taken with Subaru HSC, which is a wide-field CCD camera attached to the prime-focus of the Subaru telescope ([Miyazaki et al. 2018](#)). The HSC has a wide field of view of 1.5° diameter with 116 full-depletion CCDs which have a high sensitivity up to $1\text{ }\mu\text{m}$. The NB816 filter has a transmission-weighted mean wavelength of $\lambda = 8177\text{\AA}$ and $\text{FWHM} = 113\text{\AA}$, suitable to detect Ly α emission lines at $z = 5.726 \pm 0.046$. The filter transmission curves are shown in Figure 3. The z -band photometry is not used for the LAE candidate selection, but images are used for the visual inspection. The observations were performed in 2019-2020 in queue mode. The single exposure takes ~ 200 seconds for broad bands, and 600 seconds for NB816. Exposures were taken at different position angles on the sky around the quasar position to reduce the difference in sensitivity within the field of view as much as possible. The details of the observations and the imaging data are summarized in Table 2.

The data were processed using HSC pipeline version 6.7 (*hscpipe*; [Bosch et al. 2018](#)). The *hscpipe* first performs detrending, and calibrates the coordinate and flux using known objects in each shot.

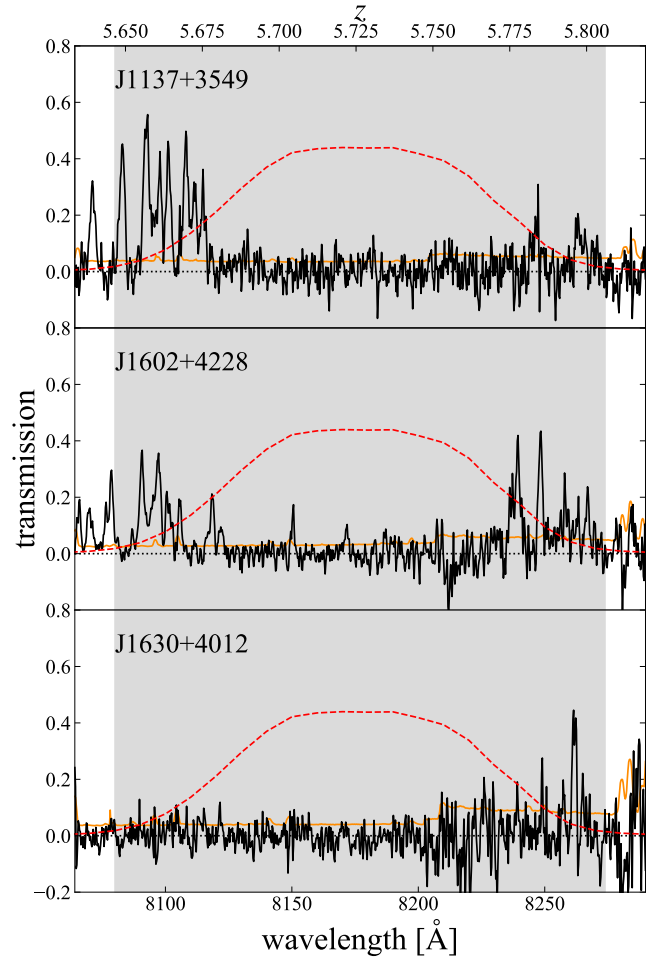


Figure 2. The transmission curves of quasar spectra. The orange lines represent the spectral noise. The grey regions indicate the wavelength range corresponding to the $50 h^{-1}$ Mpc range, used for the measurement of τ_{eff} . The red lines present the NB816 transmission curve.

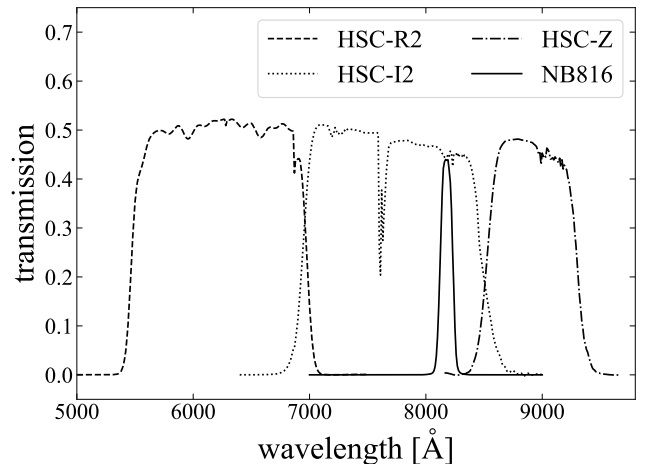


Figure 3. The transmission curves for the filter HSC-R2, HSC-I2, HSC-Z, and NB816. Area-averaged transmission data are plotted.

Table 2. Summary of Observations and Imaging Data

Field	Filter	Exp. time [hr]	PSF size ["]	$m_{5\sigma}^a$	Observation date
J1137+3549	HSC-R2	0.7	0.85	26.6	2020 Feb. 28 ^b
	HSC-I2	1.2	0.81	26.1	2019 Apr. 9 ^b , May. 1 ^b , 2020 May. 28 ^b
	HSC-Z	2.0	0.77	25.7	2019 Mar. 16 ^b , 2020 Jun. 22 ^b
	NB816	2.0	1.02	25.4	2019 Mar. 31
J1602+4228	HSC-R2	2.1	0.80	26.8	2019 Jun. 11 ^b , 2020 Feb. 23 ^b , 2020 May. 19 ^b
	HSC-I2	1.8	0.59	26.3	2019 May. 29 ^b , Jun. 8, 9, 2020 May. 20 ^b
	HSC-Z	2.0	0.76	25.8	2019 Mar. 16 ^b , 2020 Jun. 22 ^b
	NB816	1.0	0.57	25.2	2019 Apr. 9
J1630+4012	HSC-R2	2.1	1.04	26.6	2019 Jun. 11 ^b , 2020 May. 19 ^b
	HSC-I2	1.5	0.76	26.2	2019 May. 29 ^b
	HSC-Z	2.0	0.61	25.5	2019 Mar. 16 ^b , 2020 Jun. 22 ^b
	NB816	2.0	0.62	25.5	2019 Mar. 31, Apr. 9

^a the median of 5σ limiting magnitude of each patch.

^b These data are shared with another program by Kashino et al.(in prep.)

Table 3. Summary of the flags for the LAE selection

Flag	Value	Comment
detect_is_tract_inner	True	Object is located closer to the center compared to adjacent tract images
detect_is_patch_inner	True	Object is located closer to the center compared to adjacent patch images
base_PixelFlags_flag_edge	False	Source is outside usable exposure region
base_PixelFlags_flag_interpolatedCenter	False	Interpolated pixel in the Source center
base_PixelFlags_flag_saturatedCenter	False	Saturated pixel in the Source center
base_PixelFlags_flag_bad	False	Bad pixel in the Source footprint

Then it combines images from different exposures and performs detection and photometry of objects. We apply "forced" photometry, in which photometry is carried out using the centroid coordinate of the reference band for all bands. The reference band is NB816 in this study. The total magnitudes and colors are evaluated by `convolvedflux_2_15`, which corresponds to $1''.5$ aperture magnitude after an aperture correction. We use some flags to exclude objects which saturate or are affected by bad pixels. These flags are summarized in Table 3.

We determine the mask regions in addition to the mask defined in *hscpipe* described above. We build a star sample brighter than 18 mag in *G*-band from the *Gaia* Data Release 2 (DR2) (Gaia Collaboration et al. 2016, 2018). We mask regions around the bright stars and exclude the objects which exist in the masks. The radii of the mask, r , are calculated using the following equation (Coupon et al. 2018):

$$r ["] = \begin{cases} 708.9 \times \exp(-G_{\text{Gaia}}/8.41), & (G_{\text{Gaia}} < 9) \\ 694.7 \times \exp(-G_{\text{Gaia}}/4.04), & (G_{\text{Gaia}} \geq 9) \end{cases}, \quad (7)$$

where G_{Gaia} is *G*-band magnitude from *Gaia* DR2. We check the final images and set additional masks covering the regions affected by cosmic ray or CCD malfunction. We calculate the survey area of each field by generating 100 random points per arcmin² and counting the number of the random points out of the masked regions. The survey area are 5094, 5025, and 4826 arcmin² for J1137+3549, J1602+4228, and J1630+4012, respectively.

We divide the whole observed area of each field into small square regions, which is called a *patch*, and measure the limiting magnitude in each *patch*, following Inoue et al. (2020). We conduct $1''.5$ aperture photometry at 5000 random positions per *patch* avoiding

masked regions and the objects detected by `SExtractor` version 2.8.6 (Bertin & Arnouts 1996) in advance. The standard deviation, σ , of the $1''.5$ aperture photometry was obtained from the histogram of the background-subtracted aperture counts by fitting a Gaussian function. The 5σ limiting magnitudes of each field are shown in Figure 4.

2.4 LAE selection

LAE candidates are selected using the following criteria from Shibuya et al. (2018):

$$\begin{aligned} & \text{NB816} < \text{NB816}_{5\sigma}, \\ & i - \text{NB816} > 1.2, \text{ and} \\ & r > r_{3\sigma} \text{ or } r - i > 1.0, \end{aligned} \quad (8)$$

where the subscript $n\sigma$ indicates the $n\sigma$ limiting magnitude. The median values of limiting magnitude measured in each *patch* are used for the selection. The *i*-band magnitudes fainter than 2σ limiting magnitude are replaced with 2σ limiting magnitude. The criterion of $i - \text{NB816} > 1.2$ in Equation 8 corresponds to the rest-frame Ly α equivalent width $\text{EW}_0 \gtrsim 10 \text{ \AA}$. In addition to the criteria described above,

$$i - \text{NB816} > 3\sigma_{i-\text{NB816}} \quad (9)$$

is also used for the selection. The $3\sigma_{i-\text{NB816}}$ is the 3σ error of $i - \text{NB816}$ color as a function of the *NB816* flux, given by

$$3\sigma_{i-\text{NB816}} = -2.5 \log_{10} \left(1 - 3 \frac{\sqrt{f_{1\sigma, \text{NB816}}^2 + f_{1\sigma, i}^2}}{f_{\text{NB816}}} \right), \quad (10)$$

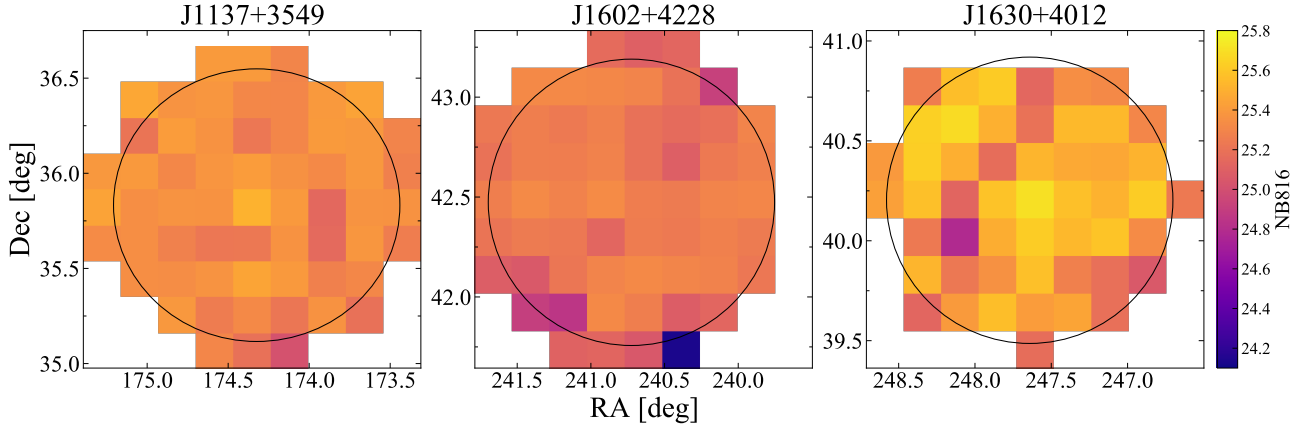


Figure 4. The maps of 5σ limiting magnitude of NB816 in the fields of J1137+3549, J1602+4228, and J1630+4012 (from left to right), respectively. The black circles indicate the field of view in each field.

where $f_{1\sigma, NB816}$ and $f_{1\sigma, i}$ are the 1σ flux error in the NB816 and i band photometry, respectively. Finally, we perform visual inspections for the all LAE candidates selected by the criteria above, in order to reject the objects affected by cosmic ray or bad pixels, noise features in the outskirts of bright objects. The resultant number of LAE candidates are 84, 80, and 97 for the fields of J1137+3549, J1602+4228, and J1630+4012, respectively. Objects from the final LAE candidates are plotted in the NB816 vs. i - NB816 diagram, shown in Figure 5.

To estimate the completeness of the LAE selection, we randomly distribute 100 mock LAEs per 0.5 mag per patch in observed images using BALROG². We assume a model LAE spectrum with a flat continuum ($f_\nu = \text{const.}$) and a Ly α emission included as a δ -function. The EW₀ distribution of Ly α emission is distributed to be consistent with that of Shibuya et al. (2018), and the IGM absorption from Madau (1995) is adopted. The redshift of LAEs is fixed at $z = 5.7$. We confirmed that the completeness estimates do not significantly change within the observational error when the redshift of the random sources follow the distribution corresponding to the NB816 transmission curve. In BALROG workflow, object simulations are performed by GALSIM (Rowe et al. 2015). The mock LAEs have a Sérsic index of $n = 1.5$ and a half-light radius of $r_c \sim 0.9$ kpc, corresponding to 0.15 arcsec for LAEs at $z = 5.7$ (Konno et al. 2018). The BALROG uses point spread functions calculated by PSFEx (Bertin 2011) from observed images. Then we detect the objects and measure photometry with *hscpipe*, the same way as the detection procedure of observed LAEs. We apply the same selection criteria of LAEs as described in Equations 8 and 9. We performed this procedure for ~ 70 patches per region. The medians of measured completeness are shown in Figure 6.

Figure 7 shows the surface number density of LAEs. We corrected for the raw surface number density using the completeness measured in each patch. The average surface number density after the completeness correction are slightly smaller than those from Konno et al. (2018) and Ono et al. (2021) at NB816 < 25 mag, though the discrepancy is within the range of field-to-field variation, shown by Ono et al. (2021) for five HSC field of views.

3 RESULTS

We calculate the LAE surface number density Σ_{LAE} of each field, by summing all LAEs' contribution calculated using 2D Gaussian kernel as $K(\mathbf{X}_i, \mathbf{X}_0)$:

$$K(\mathbf{X}_i, \mathbf{X}_0) = \frac{1}{2\pi b^2} \exp\left(-\frac{r(\mathbf{X}_i, \mathbf{X}_0)^2}{2b^2}\right), \quad (11)$$

where b is the bandwidth parameter and $r(\mathbf{X}_i, \mathbf{X}_0)$ is the angular distance between two positions. We apply a constant bandwidth $4'$. The maps are constructed through a 128×128 grid for each field. If the area within $8'$ from a point is covered by a masked region more than 50 %, we exclude the point from the density map. The galaxy overdensity δ_{LAE} is defined as

$$\delta_{\text{LAE}} = \frac{\Sigma_{\text{LAE}} - \langle \Sigma_{\text{LAE}} \rangle}{\langle \Sigma_{\text{LAE}} \rangle}, \quad (12)$$

where $\langle \Sigma_{\text{LAE}} \rangle$ is the mean surface number density of each field. The overdensity map (color contour), as well as the sky distribution of LAEs (red dots) are shown in Figure 8. The measured number densities are corrected using selection completeness maps, which are shown in Figure 9, taking into account the spatial biases of the sensitivity. The detail of the estimate of the selection completeness is described in Section 2.4. We construct completeness maps, weighting the completeness for each magnitude down to the 5σ limiting magnitude of NB816. The contribution of each mock galaxy is smoothed using Equation 11.

The overdensity maps corrected for the sensitivity variation are shown in Figure 10. The mean corrected number density of LAEs brighter than 5σ limiting magnitude are 0.018, 0.018, 0.023 arcmin⁻², for the J1137+3549, J1602+4228, and J1630+4012 field, respectively. Figure 10 shows that there is a large variation of $z = 5.7$ LAE densities between the three fields. The LAE density near the quasar sightline is high in the J1137+3549 and J1602+4228 fields, while it is low in the J1630+4012 field. The overdensities directly above the quasar sightline are $\delta_{\text{LAE}} = 1.54, 1.28, 0.33$ for the J1137+3549, J1602+4228, and J1630+4012 fields, respectively.

Figure 11 shows the surface density of LAEs as a function of projected distances from the quasar sightline. The profiles for the J1137+3549 and J1602+4228 fields show a remarkable tendency to rise toward the center, while that for the J1630+4012 field shows a trend that decreases toward the center except for the innermost bin.

² <https://github.com/emhuff/Balrog>

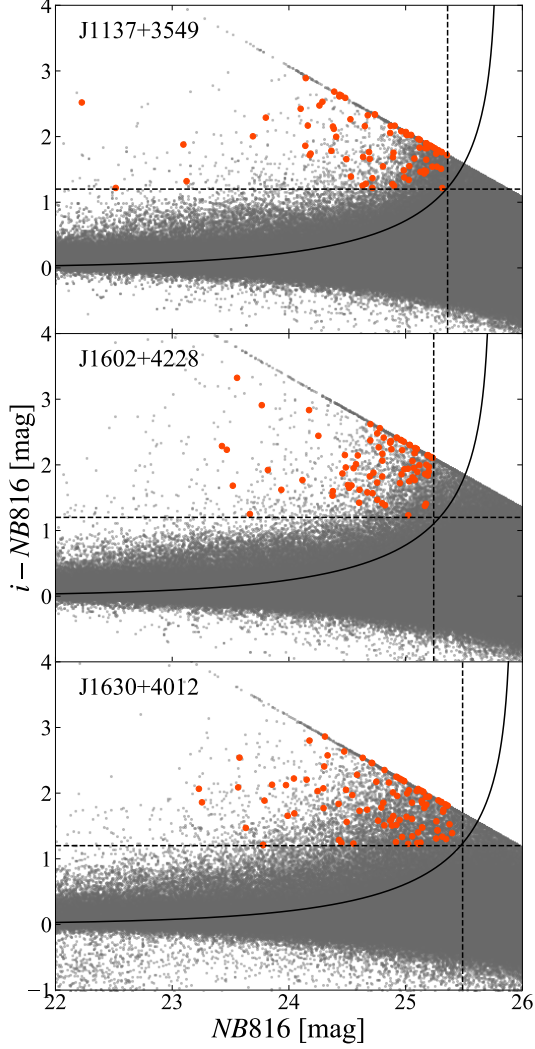


Figure 5. The $NB816$ vs. $i - NB816$ diagram of each field. The LAE candidates and all detected sources are shown in red and grey dots, respectively. The horizontal dashed lines indicate $i - NB816 = 1.2$ and the vertical dashed lines indicate the median of $NB816_{5\sigma}$ measured in each patch. The solid curves indicate Equation 9.

The 5σ limiting magnitude of $NB816$ varies up to ~ 0.3 mag among the three fields. Fixing the limiting magnitude does not change the overall trend, as shown in Appendix A. The number densities are consistent with each other at $> 20 h^{-1}\text{Mpc}$ bins in the J1137+3549 and J1602+4228 fields, and at $> 40 h^{-1}\text{Mpc}$ in the J1630+4012 field. The statistical significance of over(under) densities calculated within $20 h^{-1}\text{Mpc}$ from quasar sightline are 2.3σ , 2.7σ , and 1.3σ , respectively, where σ is the rms of the fluctuation in the field of view of the number density within an aperture of the same size. In the J1630+4012 field, the overdensity directly above the sightline is close to the mean, but when the overdensity is calculated in $< 40 h^{-1}\text{Mpc}$, it yields $\delta_{\text{LAE}} = -0.26$, suggesting the LAE deficit.

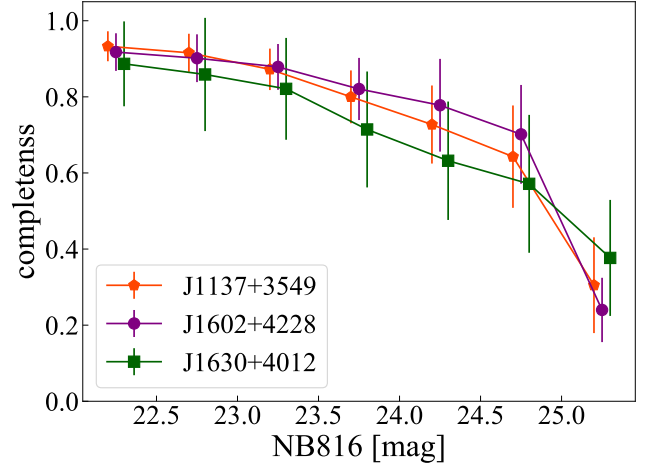


Figure 6. The LAE selection completeness in each field. The median values of measured patches are plotted. The error bars indicate the Poisson errors. The data points are slightly shifted horizontally for clarity.

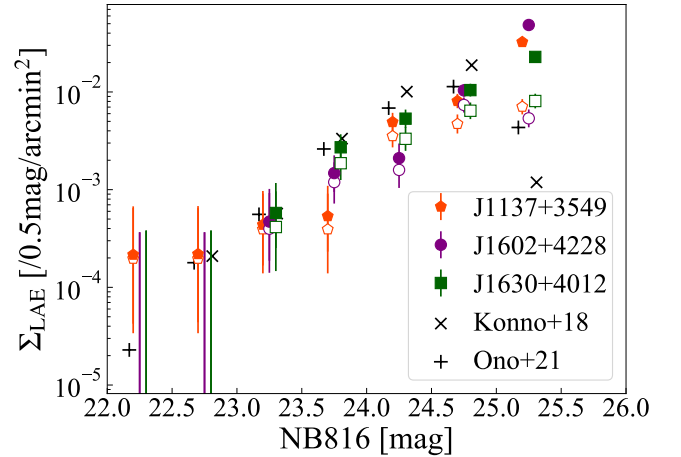


Figure 7. The surface number density of the LAEs with 1σ Poisson error in each field. The orange pentagons, purple circles, and green squares indicate the surface number densities in the fields of J1137+3549, J1602+4228, and J1630+4012, respectively. The open and filled symbols show raw and completeness-corrected surface density, respectively. The black points show the surface number density from Konno et al. (2018) and Ono et al. (2021). The data points are slightly shifted horizontally for clarity.

4 DISCUSSION

4.1 Uncertainties of the optical depth measurement

We have described the τ_{eff} measurement in Section 2.2, but due to the noisy spectra and the difficulty in calibration of high-resolution spectra, the uncertainties of τ_{eff} may not be small. In this section, we assess the robustness of the τ_{eff} measurement by several methods.

First, We estimate upper limits on τ_{eff} , using only the flux of prominent peak transmission, since the overall flux must be equal to or greater than flux in the peaks. The flux in 8080-8140, 8176-8183, 8243-8248, and 8261-8271 Å for J1137+3549, 8086-8108, 8115-8125, 8148-8152, 8168-8174, 8235-8242, and 8247-8274 Å for J1602+4228, and 8115-8123, 8259-8263 Å for J1630+4012 are used,

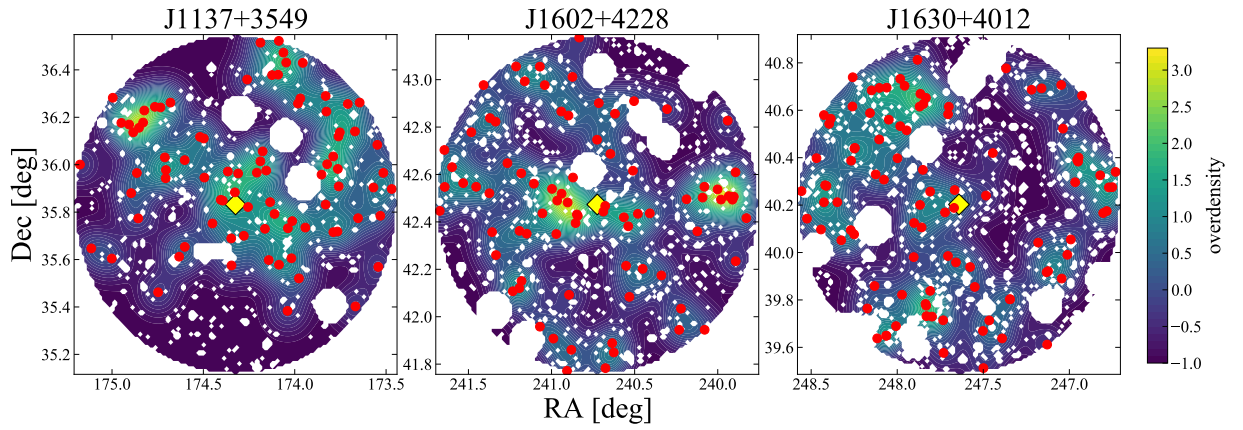


Figure 8. The LAE overdensity maps. Red points show LAE candidates and the yellow diamonds show quasar sightlines. The masked regions are shown as the white areas.

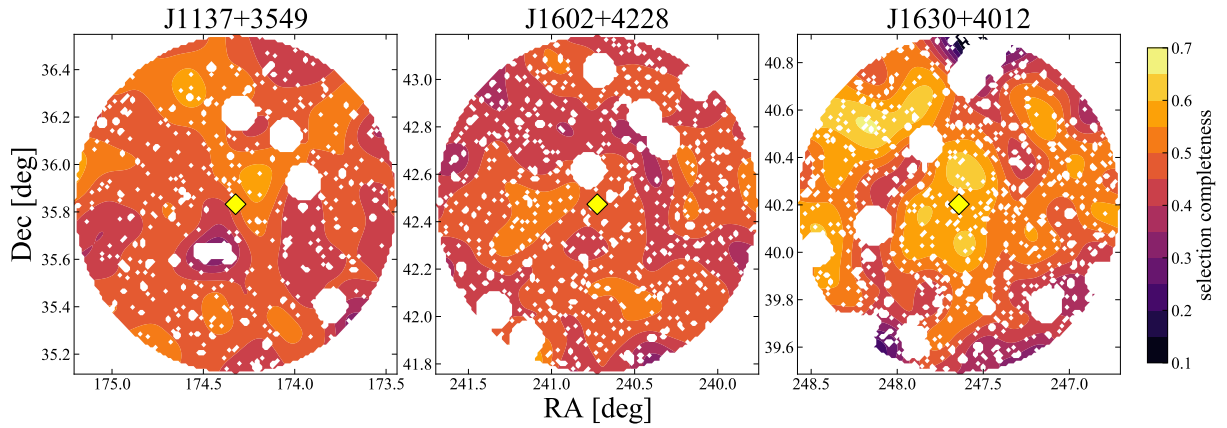


Figure 9. The selection completeness maps. The yellow diamonds show quasar sightlines.

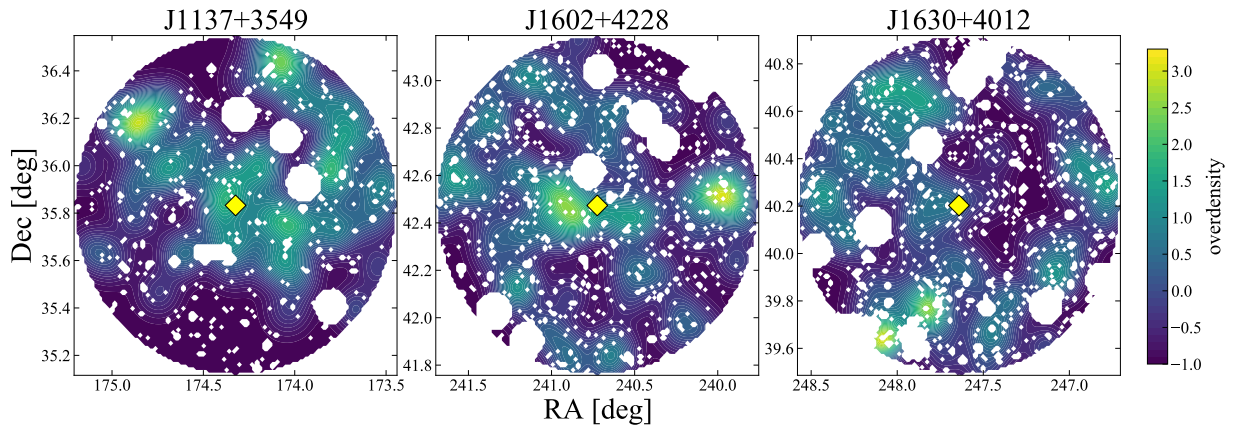


Figure 10. The overdensity maps corrected by the selection completeness maps. The yellow diamonds show the quasar sightlines.

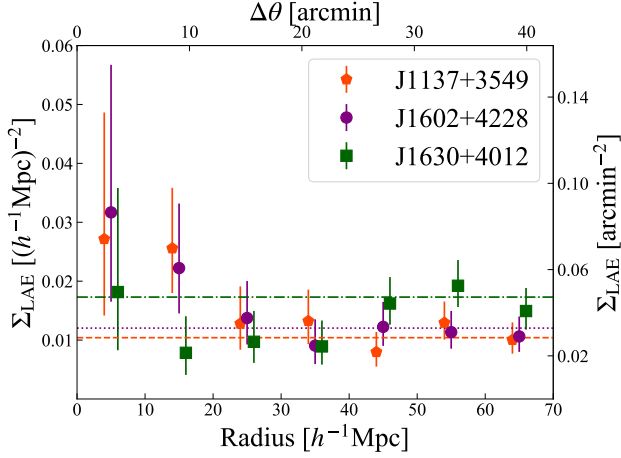


Figure 11. The surface density of LAEs as a function of projected distances from the quasar sightline. The orange pentagons, purple circles, and green squares indicate the surface number densities with 1σ Poisson errors in the fields of J1137+3549, J1602+4228, and J1630+4012, respectively. The horizontal dashed, dotted, and dashed-dotted lines show the mean surface density at $> 40h^{-1}\text{Mpc}$ in the fields of J1137+3549, J1602+4228, and J1630+4012, respectively. The data points are slightly shifted horizontally for clarity.

and for the rest in NB816 coverage, the flux is replaced with zero. We confirm these wavelength ranges are free from sky OH emissions (Osterbrock et al. 1996). We find the upper limits of $\tau_{\text{eff}} \leq 3.04$ for J1137+3549, ≤ 3.21 for J1602+4228, and ≤ 5.30 for J1630+4012.

Another way to check the τ_{eff} measurement is using the NB816 and z-band $1''.5$ aperture photometry at the quasar sightline. We use the z-band photometry to estimate the unabsorbed continuum flux at NB816 wavelength by using the intrinsic spectra estimated by PCA to be compared with the observed NB816 flux. This calculation finds $\tau_{\text{eff}} = 3.61 \pm 0.03$, and 5.48 ± 0.40 for J1137+3549 and J1630+4012, respectively. This method could not be applied to J1602+4228 because there is an object with comparable-brightness near the quasar sightline, which blended with the quasar image in the z-band, and the accurate continuum flux can not be measured.

Finally, as mentioned in Section 2.2, τ_{eff} measurements do not rely much on continuum estimation, but for Keck ESI echelle data, it is very difficult to calibrate the zero point correctly, especially for noisy spectra. To investigate the effect of uncertainty of the zero point of quasar spectra, we calculate τ_{eff} with changing zero point by 1% of the continuum flux. Increasing (decreasing) zero point gives us $\tau_{\text{eff}} = 3.31 \pm 0.05$ (2.87 ± 0.3) for J1137+3549, 3.52 ± 0.05 (3.01 ± 0.03) for J1602+4228, and ≥ 5.44 (4.25 ± 0.18) for J1630+4012. Note that this zero point uncertainty can independently add to the uncertainties of the above two τ_{eff} evaluations.

In summary, each measurement agrees almost consistently with the others: the τ_{eff} of J1137+3549 and J1602+4228 are ~ 3 , while the τ_{eff} of J1630+4012 is $\tau_{\text{eff}} \sim 5.5$, although there are non-negligible uncertainties.

4.2 Comparison with the models

A deficit of galaxies is predicted at the sightline with deep Ly α trough based on the Γ model, while in quite contrary, an overdensity of galaxies is predicted based on the T model. This study found that LAE underdensity around a high τ_{eff} region and overdensities

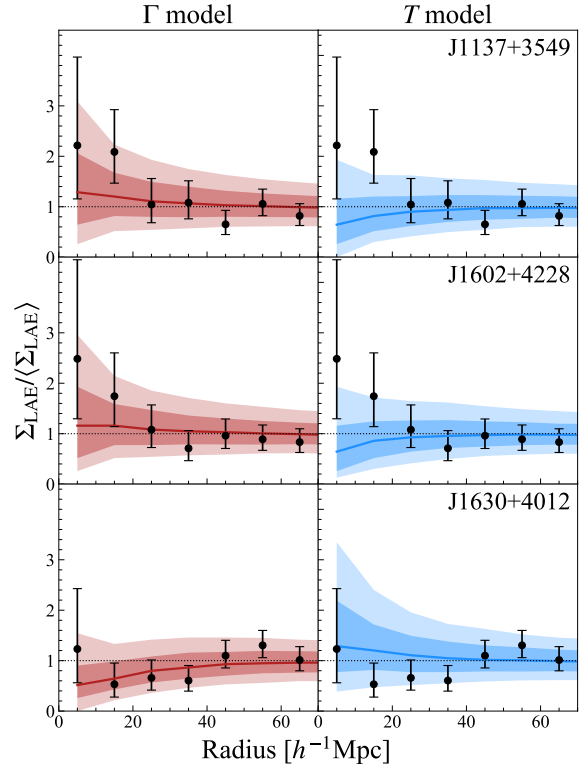


Figure 12. The surface density of LAE candidates normalized by the mean density in each field, as a function of projected distances from the quasar sightline. The error bars indicate 1σ Poisson errors. The red and blue lines show the mean model predictions for the Γ model and the T model for fields surrounding $50 h^{-1}\text{Mpc}$ sightline for each observed central τ_{eff} . The dark and light shaded regions indicate the 68% and 95% ranges from random trials from the model predictions.

around low τ_{eff} regions at $z = 5.7$, being qualitatively consistent with the Γ model; however, a more quantitative comparison is needed. In this section, we compare our observations with various reionization models.

4.2.1 Γ model and T model

We compare the observational results with the model predictions of Davies et al. (2018), which provides model predictions of their radial distribution of Σ_{LAE} for various central τ_{eff} for the Γ and T models. The model that we used here is almost identical to the one in their original paper, but in order to match our observations as closely as possible, we asked them to change the limiting magnitude from their original of $\text{NB816} = 26.0$ to $\text{NB816} = 25.5$, which is almost the same as the limiting magnitude of the observed data, $\text{NB816} = 25.2 - 25.5$ mag. We note that the detection completeness in the model is assumed to be 100% down to this limit, which makes the uncertainty of the predictions smaller than that of the actual observation. This model assumes the IGM τ_{eff} measurement over sightline $50 h^{-1}\text{Mpc}$, corresponding to $z = 5.65 - 5.81$. However, it should be noted that the observed LAE density is weighted by the transmission rate of the NB816. Therefore, what should be exactly compared to this LAE density is the model prediction based on τ_{eff}

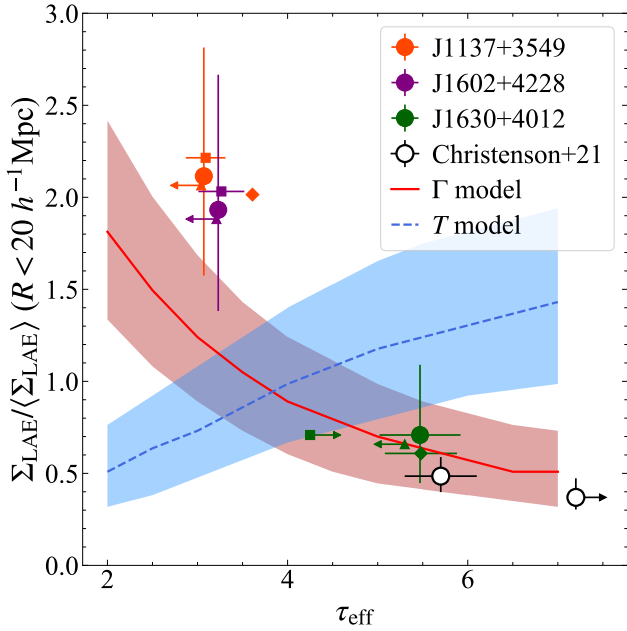


Figure 13. The relation between τ_{eff} and LAE density within $20 h^{-1} \text{Mpc}$ from the quasar sightline. The red and blue lines indicate the model predictions of the Γ model and the T model with the 68% ranges from random trials shown by the shaded regions as in Figure 12. The filled circles show the τ_{eff} measurements for J1137+3549 (orange), J1602+4228 (purple), and J1630+4012 (green), respectively. The open circles indicate the measurements of Christenson et al. (2021). The triangles, diamonds, and squares show the τ_{eff} upper limit using peak flux, τ_{eff} from photometry, and τ_{eff} when changing the zero point by ± 0.1 mag, respectively, and are slightly shifted vertically for clarity. The vertical error bars present 1σ Poisson errors.

weighted by NB816 transmission rate, which is not exactly the same as their $50 h^{-1} \text{Mpc}$ model.

Figure 12 shows the surface density of LAEs normalized by the mean density in each field as a function of projected distances from the quasar sightline, along with the model predictions based on the Γ model (Davies & Furlanetto 2016) and the T model (D’Aloisio et al. 2015). The model predictions assume LAEs down to $\text{NB816} = 25.5$ and the observed τ_{eff} measured at each quasar sightline. The profiles for the J1137+3549 and J1602+4228 fields are rather consistent with the Γ model. However, the model predictions have large uncertainties and are too similar to distinguish at the τ_{eff} of J1137+3549 and J1602+4228. All the data points are consistent with both model predictions within the errors. The central τ_{eff} here is simply measured in the range of $50 h^{-1} \text{Mpc}$ for both the observation and the model; therefore, a more detailed τ_{eff} measurement that takes NB transmissions into account, as was done for LAE selection, might be a more effective way of testing these models. The profile for the J1630+4012 field, whose overall trend is to decrease toward the center, is consistent with the prediction by the Γ model. The excessively large relative density in the central region in the two low- τ_{eff} fields may be due to either the intrinsic large-scale structure (see Sec. 4.3) or the small number density of galaxies selected in the entire field of view.

In summary, the observed data in the three regions taken together appear to favor the Γ model, but the T model cannot be completely ruled out due to the large observation errors and the scatters in the model predictions.

Figure 13 shows the relation between τ_{eff} at the quasar sight-

line and the LAE density around it within $20 h^{-1} \text{Mpc}$. The points represent the τ_{eff} estimated by several ways described in Sec 4.1. Although there are variations in the measured τ_{eff} , the LAE density in the J1630+4012 field is suggestive of the Γ model. In the case of J1137+3549 and J1602+4228, the observed LAE density is larger than either model, but more consistent with the Γ model; the T model prediction is well below the observed point. It should be noted that with this degree of high and low- τ_{eff} of our sample, it is somewhat difficult to distinguish the two models. Together with previous observations (Christenson et al. 2021) for other two high- τ_{eff} regions, we conclude that the overall observational results are well consistent with the Γ model.

One of the major factors giving ambiguity to the conclusion is the τ_{eff} uncertainty. As can be seen in Figure 1, the Gunn-Peterson troughs of our sample are not long enough to cover the whole transmission wavelengths of the NB816 filter, unlike that of J0148+0600, which has an exceptionally long trough. The τ_{eff} uncertainty is small, if the trough is sufficiently long, as in J0148+0600, whereas, it is difficult to measure the appropriate τ_{eff} in three regions targeted by this study where there are fine structures of the IGM transmission in the NB816 wavelength range. When we measure the τ_{eff} of J1137+3549 and J1602+4228 considering the exact NB816 transmission curve, their τ_{eff} turn out to be as high as ~ 5 , and consequently, it could alter our statistical conclusions in comparison with the models. It is hard to come to a clear conclusion until we measure the redshifts of galaxies around the sightlines. On the other hand, τ_{eff} fluctuations due to unstable IGM transmission in the filter wavelength range also dilute the τ_{eff} -galaxy density relation in the model predictions. In the sense, the τ_{eff} value predicted by the model to be compared with should be calculated taking into account the NB filter transmission, which would significantly affect the observed redshift distribution of LAEs. Nevertheless, we would like to emphasize that, in Figure 12 and 13, the τ_{eff} for both the observation and the model are measured in the $50 h^{-1} \text{Mpc}$ range, making them an appropriate comparison.

To avoid the influence of this τ_{eff} uncertainty, it is ideal to select almost perfect opaque/transparent regions over $>50 h^{-1} \text{Mpc}$. Several quasar sightlines with significantly long ($>80 h^{-1} \text{Mpc}$) troughs have been found recently (Zhu et al. 2021). However, the number of such sightlines is still small, and even smaller if we further restrict the number to those that fit the NB wavelength range; therefore, it is challenging to increase the size of ideal sample. Another way to overcome the problem is to make more detailed model predictions according to the small scale τ_{eff} fluctuations, which are involved in the large model uncertainties, though as discussed later, even this is taken into account, cosmic variance or LAE bias can make it difficult to distinguish the two models. Third, spectroscopic observation of all LAEs around sightlines will clearly reveal the relation between LAE density and IGM transmission in sightline direction. Spectroscopic follow-up of all the LAEs is very expensive now, but will become much easier in future with next-generation large multi-object spectrographs such as the Prime Focus Spectrograph (PFS) on the Subaru Telescope or the Multi-Object Optical and Near-infrared Spectrograph (MOONS) on the Very Large Telescope (VLT).

It is interesting to compare with an observational result by Meyer et al. (2020), who detected $2-3\sigma$ excess of Ly α transmission spikes on the sightlines of background quasars on scales $10-60 \text{cMpc}$ around spectroscopically confirmed galaxies; however, they also found that some large transmission spikes are not associated with any detected galaxy. Both Γ and T may contribute to the fluctuation of τ_{eff} , and perhaps the contribution varies from place to place, so that even in similarly high- τ_{eff} region, the galaxy densities could be different. The question is what determines whether Γ or T is dominant for a given

place, but that is not clear from this study alone. The process of reionization may be more complicated than we thought, if fluctuations in Γ and T and neutral islands all come into play. The overdensities of J1137+3549 and J1602+4228 near the sightlines are much higher than expected for their τ_{eff} (Figure 13), so factors other than the reionization process may be at play. It is increasingly important to examine multiple fields like this study.

4.2.2 Late ionization model

Like the Γ model, the late ionization model also predicts galaxy deficit in high τ_{eff} regions (Nasir & D’Aloisio 2020; Keating et al. 2020a), which is consistent with our observational result of J1630+4012. It is difficult to distinguish the late reionization model, whose mean LAE surface density profile for opaque sightlines should generally show underdensity, from the Γ model. Interestingly, Keating et al. (2020a) suggested that, in the late reionization model, the underdense regions corresponds to high- τ_{eff} regions only before the neutral islands have been ionized, and after that these hot, recently reionized voids should instead correspond to the low- τ_{eff} regions. This is in clear contrast with the Γ model, whose low- τ_{eff} sightlines almost always correspond to overdensities. Our observational results for low- τ_{eff} regions in the J1137+3549 and J1602+4228 fields show apparent overdensities around the sightlines, which is naively consistent with the Γ model, and likely to be inconsistent with the late reionization model. However, Nasir & D’Aloisio (2020) suggested that some of the most transmissive regions in the late reionization model should actually correspond to the deficit of LAEs, but they are relatively rare, and something similar could be observed even in the Γ model. Based on their model, both the Γ model and the late reionization model predict galaxy densities with large scatter in the low- τ_{eff} region, so it is difficult to distinguish between the two models, even in the low- τ_{eff} region. The LAE radial distribution based their model including the reionization temperature fluctuation shows a larger scatter than Davies et al. (2018). Our result, which shows relatively strong correlation between low- τ_{eff} and LAE overdensity, may at least suggest that the relic temperature fluctuation does not affect reionization that much. However, the number of our low- τ_{eff} sample is limited to only two, and most of the simulations only care about the most opaque and transmissive sightlines, which does not allow for a rigorous comparison with this study. More quantitative comparisons are required in the future.

4.2.3 Quasar model

To account for the observed dispersion of τ_{eff} at $z > 5.5$, there is an alternative model, in which rare sources like quasars or AGNs could generate substantial large-scale ($\sim 50 h^{-1}$ Mpc) opacity variations (Chardin et al. 2017). If quasars exist in these fields, quasars with extremely high Ly α EWs should be detectable in our NB imaging observation. There are two such sources in the J1137+3549 field only as very bright sources with $NB816 < 23$, which could be quasar candidates. We check the existing database and they do not seem to be already spectroscopically confirmed sources. Both of them are at the edge of the field of view, one in the LAE high-density region and the other in the low-density region. Whether these are quasars or not will not be known until spectroscopy is taken. However, the strong correlation between the τ_{eff} and galaxy density, consistently seen in all the observed two low- τ_{eff} and three high- τ_{eff} sightlines (i.e., this work plus Becker et al. (2018), Kashino et al. (2020), and Christenson et al. (2021)) is rather likely to be contradict this quasar model that

predicts the lack of clear correlations between them. In addition, their model assumes a high number density of quasars with $\sim 10^{-6} \text{ Mpc}^{-3}$ based on Giallongo et al. (2015), which is in contradict with some measurements (Kashikawa et al. 2015; Onoue et al. 2017; Matsuoka et al. 2019; Jiang et al. 2022), and is also in tension with constraints on the He II reionization (Worseck et al. 2014).

4.3 LAE large-scale spatial bias

As seen in Figure 13, the overdensities in the vicinity of the sightlines in the J1137+3549 and J1602+4228 fields are higher than the Γ model prediction. This indicates that there may be factors other than the reionization process. We have detected LAEs at $z = 5.726 \pm 0.046$, where the Ly α emission lines are easily detected by the NB816 imaging observations under the assumption that LAEs are representative galaxies at the epoch. However, if there is some bias in the spatial distribution of LAEs and they do not represent the average galaxy distribution in the universe, we cannot expect to see the relationship between Ly α opacity and LAE local density as expected from the theoretical models. Some studies indicated physical similarities between LAEs and non-LAEs (Hathi et al. 2016; Shimakawa et al. 2017), suggesting that LAEs can be used to probe the general low mass star-forming galaxies tracing the underlying density structures, while several recent studies have pointed out that the distribution of LAE is different from the field, especially in high density regions. Recently, Ito et al. (2021) claimed that the cross-correlation signals between LAEs and star-forming galaxies are significantly lower than their auto-correlation signals up to $\sim 30 \text{ cMpc}$, suggesting that the distribution of LAEs are different from those of general galaxy populations. Toshikawa et al. (2016) showed that the Ly α EW is systematically low in high-density regions of LBG, suggesting possible Ly α suppression in galaxy overdense regions. Shimakawa et al. (2017) have found a LAE number deficit in a protocluster core composed of H α emitters at $z = 2$ on scales of \sim a few Mpc. Shi et al. (2019) also found a spatial offset of \sim a few tens of Mpc between the density peak of LAEs and LBGs, suggesting their different age or different dynamic stages. Cai et al. (2017), Momose et al. (2021), and Liang et al. (2021) showed LAEs tend to avoid the highest H I density regions. More recently, Huang et al. (2022) conducted a LAE search around the *Hyperion* protocluster at $z \sim 2.47$, and found that LAE well traces the large scale structures. However, their result also suggested that Ly α emission is suppressed in the highest H I regions. These results indicate that the LAE may not be a good tracer of underlying large-scale structures. If this hypothesis is correct, it is difficult to distinguish between the Γ model and the T model using LAEs as in this study. Independent validation using another galaxy population, e.g. LBG (Kashino et al. 2020), is required.

5 SUMMARY

In this study, we conduct HSC imaging with the NB816 filter to perform a LAE search at $z \sim 5.7$ in two fields containing background quasars, whose sightlines show low Ly α optical depth ($\tau_{\text{eff}} \sim 3$) at the same redshift, and a field with high optical depth ($\tau_{\text{eff}} \sim 5.5$). Our goal is to test two conflicting models for the origin of large scatter of Ly α optical depth at $z > 5.5$. In the Γ model, the observed large τ_{eff} fluctuation is due to the fluctuation in the galaxy-dominated UV background, and low(high) galaxy density should generally be observed at high(low) τ_{eff} regions. In the T model, τ_{eff} fluctuation is due to the fluctuation in the IGM gas temperature, and high(low)

galaxy density should generally be observed at high(low) τ_{eff} regions, contrary to the Γ model.

The major results are summarized below.

(i) We estimate τ_{eff} in $50 h^{-1}\text{Mpc}$ range, using PCA continuum estimation. The resultant τ_{eff} values are 3.07 ± 0.03 , 3.23 ± 0.05 , and 5.47 ± 0.86 for J1137+3549, J1602+4228, and J1630+4012, respectively. J1137+3549 and J1602+4228 show low τ_{eff} , which are in $<17\%$ from the bottom in the τ_{eff} distribution at $z = 5.6 - 5.8$ (Bosman et al. 2022), and this work is the first to investigate galaxy density in such low τ_{eff} regions. In contrast, J1630+4012 shows high τ_{eff} , which exceeds the 95% range in τ_{eff} distribution predicted by the uniform UV background model (Becker et al. 2015b) and cannot be explained by the density variations alone. We evaluate the uncertainties of the τ_{eff} measurement in several ways. Each measurement agrees almost consistently with the others: the τ_{eff} of J1137+3549 and J1602+4228 are ~ 3 , while the τ_{eff} of J1630+4012 is ~ 5.5 , although there are non-negligible uncertainties.

(ii) The numbers of LAE candidates are 84, 80, and 97 for the field of J1137+3549, J1602+4228, and J1630+4012, and the survey area is 5094, 5025, and 4826 arcmin², respectively. We map the spatial distributions of LAE candidates in the three fields by carefully correcting the variation of sensitivity in the field of view using mock LAEs.

(iii) LAE overdensities are found within $20 h^{-1}\text{Mpc}$ of the quasar sightlines in the J1137+3549 and J1602+4228 fields, while an LAE underdensity is found in the J1630+4012 field. These over(under)densities have the significance of 2.3σ , 2.7σ , and 1.3σ , respectively. The radial distributions of LAEs in the J1137+3549 and J1602+4228 fields have upward trends toward the quasar sightline, while that of the J1630+4012 field decreases toward the center.

(iv) We quantitatively compare the observed spatial distributions of LAEs to the predictions for the Γ model and the T model of Davies et al. (2018). The radial distribution of LAE surface number density centered on the quasar sightline of J1630+4012 is consistent with the Γ model, while the profiles for the other two fields are rather consistent with the Γ model, though the τ_{eff} values in these fields are not extreme enough to distinguish between the models, and cannot determine which model is more plausible.

(v) We, therefore, use a more robust statistic, the Ly α opacity-galaxy density relation (Figure 13): the relation between IGM τ_{eff} at the quasar sightline and the LAE density around it within $20 h^{-1}\text{Mpc}$. The results of all the three fields along with the previous observations are found to be consistent with the Γ model.

(vi) In the low τ_{eff} regions, in which relatively strong correlations between low- τ_{eff} and LAE overdensity are observed, which may suggest that the relic temperature fluctuation does not affect reionization that much. Another possibility is that LAE is not a good tracer of underlying large-scale structures and thus affects galaxy density somewhat independently from reionization.

The concern that remains in relation to the last point above is that LAE could not be used as a representative of galaxies. Although Becker et al. (2018) and Kashino et al. (2020) showed consistent results using LAE and LBG, we can not deny that LAE shows different distribution from other galaxy populations, or absorption by neutral H I changes the apparent distribution of LAEs. The search for continuum-selected galaxies, such as LBGs, in the same fields is required to confirm our findings focusing on LAEs. In some of our fields, the LBG search has also been conducted based on the similar motivation. In the future, we will compare the results of LAE and LBG in the same field and discuss the consistency between different galaxy populations.

In addition, observation of much lower- τ_{eff} regions is also needed. This study is the first to investigate the LAE density at low- τ_{eff} regions, but the τ_{eff} values are not low enough to clearly distinguish between the Γ model and the T model. Observations of low- τ_{eff} regions will give further insight into the plausible model for the physical origin of the patchy reionization. Also in the high- τ_{eff} region, only three regions have been observed, and we need to increase the number of sample to find out what is causing the difference between the fields. To obtain more conclusive results, we need to improve the model and further observations.

ACKNOWLEDGEMENTS

We appreciate the referee, George Becker, for his helpful suggestions and comments, which significantly improves the paper. We are grateful to Frederick Davies for providing the model predictions recalculated to fit our observations. We thank the *hscpipe* helpdesk for many helpful suggestions. We also thank to Satoshi Yamanaka, who kindly provided the code to measure the limiting magnitude. RI acknowledges support from JST SPRING, Grant Number JPMJSP2108. This research was supported by the Japan Society for the Promotion of Science through Grant-in-Aid for Scientific Research 21H04490.

This research is based on data collected at Subaru Telescope, which is operated by the National Astronomical Observatory of Japan. We are honored and grateful for the opportunity of observing the Universe from Maunakea, which has the cultural, historical and natural significance in Hawaii.

This work has made use of data from the European Space Agency (ESA) mission *Gaia* (<https://www.cosmos.esa.int/gaia>), processed by the *Gaia* Data Processing and Analysis Consortium (DPAC, <https://www.cosmos.esa.int/web/gaia/dpac/consortium>). Funding for the DPAC has been provided by national institutions, in particular the institutions participating in the *Gaia* Multilateral Agreement.

DATA AVAILABILITY

The data underlying this article will be shared on reasonable request to the corresponding author.

REFERENCES

- Becker G. D., Bolton J. S., Lidz A., 2015a, *Publ. Astron. Soc. Australia*, **32**, e045
- Becker G. D., Bolton J. S., Madau P., Pettini M., Ryan-Weber E. V., Venemans B. P., 2015b, *MNRAS*, **447**, 3402
- Becker G. D., Davies F. B., Furlanetto S. R., Malkan M. A., Boera E., Douglass C., 2018, *ApJ*, **863**, 92
- Bertin E., 2011, in Evans I. N., Accomazzi A., Mink D. J., Rots A. H., eds, *Astronomical Society of the Pacific Conference Series Vol. 442*, *Astronomical Data Analysis Software and Systems XX*. p. 435
- Bertin E., Arnouts S., 1996, *A&AS*, **117**, 393
- Bosch J., et al., 2018, *PASJ*, **70**, S5
- Bosman S. E. I., Fan X., Jiang L., Reed S., Matsuoka Y., Becker G., Haehnelt M., 2018, *MNRAS*, **479**, 1055
- Bosman S. E. I., et al., 2022, *MNRAS*, **514**, 55
- Cai Z., et al., 2017, *ApJ*, **839**, 131
- Carilli C. L., et al., 2010, *ApJ*, **714**, 834
- Chardin J., Haehnelt M. G., Aubert D., Puchwein E., 2015, *MNRAS*, **453**, 2943
- Chardin J., Puchwein E., Haehnelt M. G., 2017, *MNRAS*, **465**, 3429

Christenson H. M., Becker G. D., Furlanetto S. R., Davies F. B., Malkan M. A., Zhu Y., Boera E., Trapp A., 2021, *ApJ*, **923**, 87

Coupon J., Czakon N., Bosch J., Komiyama Y., Medezinski E., Miyazaki S., Oguri M., 2018, *PASJ*, **70**, S7

D’Aloisio A., McQuinn M., Trac H., 2015, *ApJ*, **813**, L38

D’Aloisio A., Upton Sanderbeck P. R., McQuinn M., Trac H., Shapiro P. R., 2017, *MNRAS*, **468**, 4691

D’Aloisio A., McQuinn M., Davies F. B., Furlanetto S. R., 2018, *MNRAS*, **473**, 560

Davies F. B., Furlanetto S. R., 2016, *MNRAS*, **460**, 1328

Davies F. B., Becker G. D., Furlanetto S. R., 2018, *ApJ*, **860**, 155

Eilers A.-C., Davies F. B., Hennawi J. F., 2018, *ApJ*, **864**, 53

Fan X., et al., 2006, *AJ*, **132**, 117

Furusawa H., et al., 2018, *PASJ*, **70**, S3

Gaia Collaboration et al., 2016, *A&A*, **595**, A1

Gaia Collaboration et al., 2018, *A&A*, **616**, A1

Giallongo E., et al., 2015, *A&A*, **578**, A83

Grazian A., et al., 2022, *ApJ*, **924**, 62

Gunn J. E., Peterson B. A., 1965, *ApJ*, **142**, 1633

Hathi N. P., et al., 2016, *A&A*, **588**, A26

Huang Y., et al., 2022, arXiv e-prints, p. arXiv:2206.07101

Inoue A. K., et al., 2020, *PASJ*, **72**, 101

Ishimoto R., et al., 2020, *ApJ*, **903**, 60

Ito K., et al., 2021, *ApJ*, **916**, 35

Jiang L., et al., 2009, *AJ*, **138**, 305

Jiang L., et al., 2022, arXiv e-prints, p. arXiv:2206.07825

Kashikawa N., et al., 2015, *ApJ*, **798**, 28

Kashino D., Lilly S. J., Shibuya T., Ouchi M., Kashikawa N., 2020, *ApJ*, **888**, 6

Kawanomoto S., et al., 2018, *PASJ*, **70**, 66

Keating L. C., Weinberger L. H., Kulkarni G., Haehnelt M. G., Chardin J., Aubert D., 2020a, *MNRAS*, **491**, 1736

Keating L. C., Kulkarni G., Haehnelt M. G., Chardin J., Aubert D., 2020b, *MNRAS*, **497**, 906

Komiyama Y., et al., 2018, *PASJ*, **70**, S2

Konno A., et al., 2018, *PASJ*, **70**, S16

Kulkarni G., Keating L. C., Haehnelt M. G., Bosman S. E. I., Puchwein E., Chardin J., Aubert D., 2019, *MNRAS*, **485**, L24

Liang Y., et al., 2021, *ApJ*, **907**, 3

Madau P., 1995, *ApJ*, **441**, 18

Matsuoka Y., et al., 2019, *ApJ*, **883**, 183

Meyer R. A., et al., 2020, *MNRAS*, **494**, 1560

Miyazaki S., et al., 2018, *PASJ*, **70**, S1

Momose R., et al., 2021, *ApJ*, **909**, 117

Nasir F., D’Aloisio A., 2020, *MNRAS*, **494**, 3080

Ono Y., et al., 2021, *ApJ*, **911**, 78

Onoue M., et al., 2017, *ApJ*, **847**, L15

Osterbrock D. E., Fulbright J. P., Martel A. R., Keane M. J., Trager S. C., Basri G., 1996, *PASP*, **108**, 277

Prochaska J. X., 2017, *Astronomy and Computing*, **19**, 27

Rowe B. T. P., et al., 2015, *Astronomy and Computing*, **10**, 121

Shen Y., et al., 2019, *ApJ*, **873**, 35

Shi K., et al., 2019, *ApJ*, **879**, 9

Shibuya T., et al., 2018, *PASJ*, **70**, S14

Shimakawa R., et al., 2017, *MNRAS*, **468**, L21

Suzuki N., Tytler D., Kirkman D., O’Meara J. M., Lubin D., 2005, *ApJ*, **618**, 592

Toshikawa J., et al., 2016, *ApJ*, **826**, 114

Worseck G., et al., 2014, *MNRAS*, **445**, 1745

Yang J., et al., 2020, *ApJ*, **904**, 26

Zhu Y., et al., 2021, *ApJ*, **923**, 223

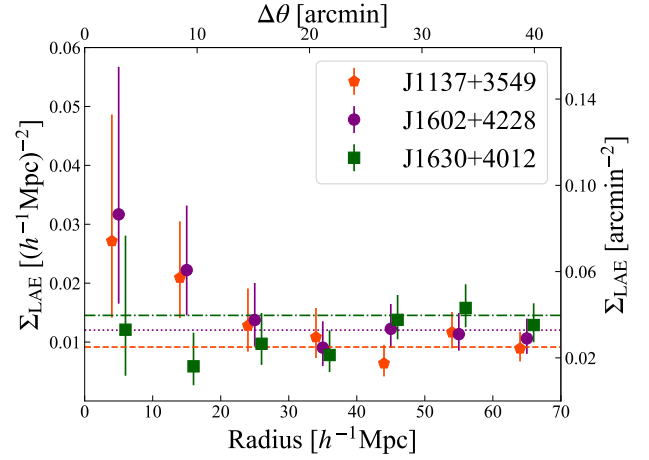


Figure A1. Same as Figure 11, but the limiting magnitude are fixed to 25.2 mag in all fields. The data points are slightly shifted horizontally for clarity.

APPENDIX A: SURFACE DENSITY OF LAES DOWN TO A FIXED LIMITING MAGNITUDE

Figure A1 shows the surface density of LAEs as a function of projected distance from the quasar sightline down to the fixed limiting magnitude of 25.2 mag, which is the shallowest among the three fields. The profiles show the similar trend to that in Figure 11, although the profiles of J1137+3549 and J1630+4012 are shifted slightly lower.

This paper has been typeset from a $\text{\TeX}/\text{\LaTeX}$ file prepared by the author.